Physica B 413 (2013) 47–54

Contents lists available at SciVerse ScienceDirect

Physica B

journal homepage: www.elsevier.com/locate/physb

Structural, thermal, optical and photoacoustic study of nanostructured $FeSb_2$ prepared by mechanical alloying

C.M. Poffo [a], J.C. de Lima [b,*], S.M. Souza [c], D.M. Trichês [c], T.A. Grandi [b], R.S. de Biasi [d]

[a] Departamento de Engenharia Mecânica, Universidade Federal de Santa Catarina, Campus Universitário Trindade, S/N, C.P. 476, 88040-900 Florianópolis, Santa Catarina, Brazil
[b] Departamento de Física, Universidade Federal de Santa Catarina, Campus Universitário Trindade, S/N, C.P. 476, 88040-900 Florianópolis, Santa Catarina, Brazil
[c] Departamento de Física, Universidade Federal do Amazonas, 3000 Japiim, 69077-000 Manaus, Amazonas, Brazil
[d] Seção de Engenharia Mecânica e de Materiais, Instituto Militar de Engenharia, 22290-270 Rio de Janeiro, RJ, Brazil

ARTICLE INFO

Article history:
Received 5 September 2012
Received in revised form
20 December 2012
Accepted 27 December 2012
Available online 3 January 2013

Keywords:
Nanocrystals
Thermoelectric materials
Mechanical alloying
X-ray diffraction
Raman spectroscopy
Photoacoustic absorption

ABSTRACT

Mechanical alloying of elemental Fe and Sb powders yielded nanostructured $FeSb_2$, an amorphous phase, along with unreacted Sb. The volume fractions of $FeSb_2$, Sb nanocrystals and interfacial/amorphous components were estimated from the X-ray diffraction pattern of the as-miller powder. The thermal stability of $FeSb_2$ was investigated by heating the powder at 250 °C and 400 °C. The XRD pattern of the sample annealed at 250 °C showed nucleation of Fe_3O_4 and decomposition of $FeSb_2$. For an annealing temperature of 400 °C, besides crystallization of the amorphous phase, the volume fractions of Sb and Fe_3O_4 increased and the volume fraction of $FeSb_2$ decreased. The optical band gap energy for samples as-milled and annealed at 400 °C was measured, and a slight decrease in the band gap was observed in the annealed sample. Thermal diffusivity parameter of the as-milled sample and of the annealed sample at 400 °C was also measured, as well as other transport properties. We also studied the contribution of the thermal diffusivity of the interfacial/amorphous component to the thermal diffusivity of the as-milled sample.

1. Introduction

It has been suggested that some strongly correlated materials have potential for thermoelectric applications at low temperatures [1–3]. This is due to the fact that the electron–electron correlations can produce large electronic densities of states at the band edges of the hybridization gap, leading to an enhancement of the absolute values of Seebeck coefficient $|S|$ [1]. $FeGa_3$ [4], FeSi [5] and $FeSb_2$ [6] are examples of strongly correlated semiconductor compounds. $FeSb_2$ and FeSi show similar physical properties in many respects [7–13].

$FeSb_2$ is a narrow direct optical band gap semiconductor [14], whose thermodynamic, thermoelectric, and magnetic properties have been widely investigated [15–19]. For example, at low temperature, it shows large Seebeck coefficient $S \approx -45000\ \mu V\ K^{-1}$, high power factor $P \approx 2300\ \mu W\ K^{-2}\ cm^{-1}$ at 12 K, a semiconducting-metallic crossover temperature of 40 K and a paramagnetic to diamagnetic crossover at around 100 K [6]). These characteristics make it a potential material for application in the cryorefrigeration field.

Under ambient conditions, $FeSb_2$ crystallizes in an orthorhombic structure (S.G. Pnnm, $Z=2$), with Fe and Sb atoms in the $2a$ (0,0,0) and $4g$ (x,y,0) Wyckoff positions, where $x=0.1885$ and $y=0.3561$, respectively. Each Fe atom is in a deformed octahedral environment, and octahedra share edges along the c-axis [20]. The $FeSb_2$ compound can be synthesized using the self-flux method [6] or the high-temperature flux method [21], among others. Recently, this compound was also produced by mechanical alloying (MA) [22].

It has been suggested by other researchers that the thermoelectric conversion efficiency can be improved by reducing the thermal conductivity without a strong degradation of the electrical properties. One way to achieve this is reducing the crystallite size of thermoelectric materials to nanometric dimensions, i.e., producing thermoelectric nanostructured materials [23]. Nanostructured materials have been produced by different techniques, including MA. Suryanarayana's paper [24] gives a good review of the MA technique, while the physical mechanisms involved are described in Refs. [25–28]

From the structural point of view, nanostructured materials have two components, one crystalline, made of crystallites with nanometric dimensions (< 1000 Å), with the same structure as the bulk counterparts, and another interfacial, made of different types of defects (grain boundaries, interphase boundaries, dislocations, etc.). Both components have similar numbers of atoms, causing a strong dependence of the properties on the atomic arrangements present in the interfacial component [29].

* Corresponding author. Tel.: +55 48 37212847; fax: +55 48 37219946.
E-mail address: fsc1jcd@fisica.ufsc.br (J.C. de Lima).

0921-4526/$ - see front matter © 2012 Elsevier B.V. All rights reserved.
http://dx.doi.org/10.1016/j.physb.2012.12.037

Using MA, we produced nanostructured $FeSb_2$ along with an amorphous phase and unreacted elemental Sb. Recently, a study at room temperature on the effect of high pressure on this as-milled powder showed the structural decomposition of the orthorhombic $FeSb_2$ phase with increasing pressure as well as the nucleation of a new high pressure tetragonal $FeSb_2$ phase [30]. Now, this as-milled powder was used to investigate its optical and photoacoustic properties at room temperature as well as its structural stability as a function of temperature. X-ray diffraction (XRD), differential scanning calorimetry (DSC), visible and infrared spectroscopy (VIS–IR), Raman spectroscopy (RS) and photoacoustic absorption spectroscopy (PAS) techniques were used. This paper reports the results of these experiments.

2. Experimental procedure

A stoichiometric $FeSb_2$ mixture of elemental powders of Fe (Aldrich, purity 99.999%) and Sb (Alfa Aesar, purity 99.999%) was sealed together with several steel balls of 11.0 mm in diameter into a cylindrical steel vial under argon atmosphere. The ball-to-powder weight ratio was 7:1. The vial was mounted on a SPEX mixer/mill, model 8000. The temperature was kept close to room temperature by a ventilation system. After 32 h of milling, the measured XRD pattern showed an excellent agreement with that given in the ICSD Database (code 41727) [20] for the orthorhombic $FeSb_2$ phase. However, the formation of an amorphous phase and unreacted elemental Sb were observed. XRD pattern was acquired using a Miniflex Rigaku powder diffractometer, equipped with CuK_α radiation ($\lambda=1.5418$ Å).

The thermal stability of the $FeSb_2$ phase and the crystallization of amorphous phase were investigated through DSC measurements, under nitrogen flow, performed in a TA Instruments 2010 DSC cell. DSC measurements using heat rates of 2.5, 5.0, 10 and 40 °C min^{-1} were carried out to calculate the activation energy to crystallize the amorphous phase.

RS spectra were measured using a Renishaw micro-Raman spectrometer, integrated with a light microscope. A laser of wavelength $\lambda=514.5$ nm was used as excitation source. Calibration of the spectrometer was performed using a single crystal silicon wafer, setting the peak at 520 cm^{-1}. The magnification of the microscope objective, time of exposure and intensity of the laser beam were 20, 120 s, and 1.0 mW, respectively.

The PAS measurements were performed on a homebuilt open photoacoustic cell (OPC) that consisted of a 250 W quartz–tungsten–halogen (QTH) lamp and a Bentham 605 current power supply. After heat filtering by a water lens, the light was mechanically chopped by a Perkin–Elmer chopper, model 197, and focused onto the sample. The sample was mounted directly in the front sound inlet of an electret microphone [31]. The output voltage from the microphone was connected to a computer through a lock-in amplifier in order to record the PAS signal amplitude and phase as functions of modulation frequency. For PAS measurements, the samples were prepared by compressing the powder with a pressure of 6 tons to form tiny circular pellets 10 mm in diameter. The thicknesses of as-milled and annealed samples were 425 and 500 μm, respectively.

3. Results and discussion

3.1. Analysis of XRD and DSC measurements of the as-milled and annealed samples

Fig. 1 shows the XRD pattern for as-milled powder (open circles) after milling for 32 h. It was compared with the patterns in the ICSD Database [20] for the Fe–Sb system, and an excellent agreement was observed with that for the orthorhombic $FeSb_2$ phase (code 41727). Diffraction peaks of unreacted elemental Sb (ICSD code 9859) and an amorphous phase were also observed. The latter will be analyzed later. The XRD pattern was refined using the Rietveld method [32], implemented in the GSAS package [33]. The structural data given in the ICSD codes were used as input data. Due to the fact that the contributions from the interfacial component and amorphous phase to the XRD pattern are diffuse and cannot be separated, they were considered as belonging to the background. The best fit was reached for the lattice parameters $a=5.8246$ Å (5.8328 Å), $b=6.5380$ Å (6.5365 Å), $c=3.2108$ Å (3.1973 Å) for $FeSb_2$; and $a=4.3003$ Å (4.3070 Å), $c=11.3088$ Å (11.2730 Å) for elemental Sb. The values between parentheses are those provided by ICSD codes. The simulated patterns and the residual intensity are also shown in Fig. 1, where an excellent agreement between simulated and experimental patterns can be seen. From the refinement, volume fractions of 93% and 7% for $FeSb_2$ and elemental Sb were obtained. Petrovic et al. [18] produced single crystal $FeSb_2$ with 8% of unreacted elemental Sb.

We developed an approach to estimate the volume fractions of crystalline and interfacial components forming the structure of the nanostructured materials. [34,35]. Here, it was used to estimate contributions of crystalline ($FeSb_2$ and Sb crystallites) and interfacial/amorphous components to the experimental XRD pattern. For converting the XRD pattern to electron units, a weighted theoretical mean square scattering factor $<f^2>_{aver} = 0.93 <f^2>_{FeSb_2} + 0.07 f^2_{Sb}$, where $<f^2>_{FeSb_2} = 1/3 f^2_{Fe} + 2/3 f^2_{Sb}$ and f^2_i is the atomic scattering factor, was calculated. From this approach, volume fractions of ≈63% and 37% for crystalline and interfacial/amorphous components were estimated, respectively. Taking into account the estimated volume fraction of interfacial/amorphous component obtained from this approach, a simple calculation yields relative volume fractions of 58.6% and 4.4% for $FeSb_2$ and unreacted elemental Sb, respectively.

When crystallites are less than approximately 1000 Å in size, appreciable broadening in the XRD peaks occurs. The peaks seen in the XRD pattern shown in Fig. 1 have their bases enlarged, indicating the presence of crystallites of very small dimensions. The average crystallite size was estimated using the Scherrer

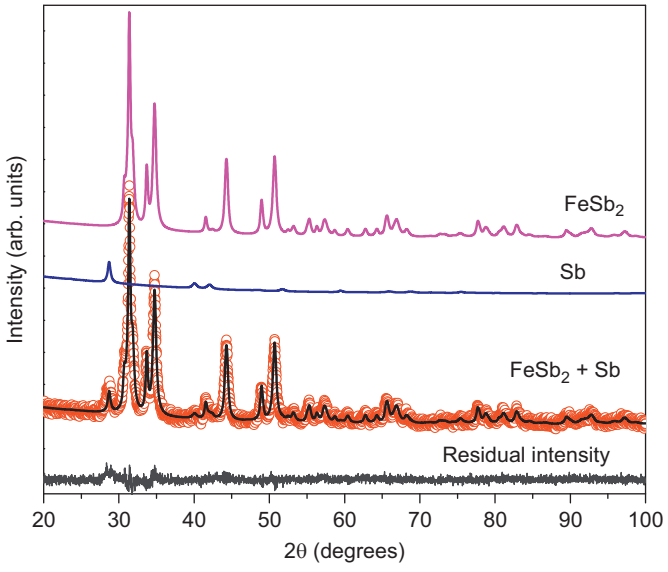

Fig. 1. Experimental (open circles) and simulated (solid lines) XRD patterns of a nanostructured powder milled for 32 h.

equation [36]

$$D = \frac{0.93\,\lambda}{\beta\cos(\theta)} \quad (1)$$

where θ is the diffraction angle, λ is the X-ray wavelength and β is the total broadening of the peak in radians, measured at the full-width at half-maximum (FWHM). From the Rietveld refinement, the β and 2θ values of the most intense peaks, located at about 31.37°, 33.72°, 34.74°, 44.29°, 48.98° and 50.70° for $FeSb_2$, were used in Eq. (1) and $D \approx 245$ Å was obtained. This value confirms that the $FeSb_2$ phase is nanostructured.

Fig. 2 shows two sequentially recorded DSC thermograms for the same as-milled sample, with a heating rate of 10 °C min^{-1}. On the first run, one can see a continuous absorption of energy up to 200 °C that is attributed to desorption of water molecules, since the as-milled powder was not pre-heated, and/or to diffusion of Fe and Sb atoms located at the interfacial component. Other two exothermic peaks located at about 198 and 336 °C are also seen. The peak at about 198 °C is attributed to the nucleation of Fe_3O_4, as will be shown later. The peak at about 336 °C is attributed to the crystallization of amorphous phase. The presence of an amorphous phase in the as-milled powder as well as its crystallization was confirmed by running a second thermogram, as shown in Fig. 2.

The activation energy E_a for the crystallization of the amorphous phase was calculated using the Kissinger equation [37]

$$\ln(B/T^2) = -E/RT + \text{constant} \quad (2)$$

where B is the heating rate, $R = 8.31447$ J mol^{-1} K^{-1} is the gas constant and T is an absolute temperature, such as the peak temperature T_p. DSC thermograms, with heating rates of 2.5, 5, 10 and 40 °C min^{-1}, were recorded and the following T_p values were obtained: 325.7 °C (2.5 °C min^{-1}), 330.0 °C (5 °C min^{-1}), 335.8 °C (10 °C min^{-1}) and 343.8 °C (40 °C min^{-1}). Using the B and T_p values shown in Eq. (2), a straight line was approximately obtained by plotting $\ln(B/T^2)$ versus $1/T$ as shown in Fig. 3. From the slope of the straight line a value of $E_a = 454.4 \pm 3.3$ kJ mol^{-1} was obtained. Finally, the crystallization mechanism may be correlated with the Avrami parameter n_A using the equation [38],

$$n_A = \frac{2.5\,R\,T_p^2}{\Delta T\,E_a} \quad (3)$$

where ΔT is the width of the crystallization at half maximum and R, T_p and E_a have already been defined. In order to obtain accurate values of ΔT, the crystallization peaks on the DSC thermograms recorded with different heating rates were fitted using a Gaussian function and the Origin software [39]. An average value for the Avrami parameter of $n_A \approx 1.0$ was obtained, suggesting that the distribution of nucleation sites is non-random and the growth may be restricted to one dimension.

Taking into account the DSC thermogram recorded in the first run, two batches of the as-milled powder were used for annealing. The powder was pressed into two pellets, which were sealed in quartz tubes evacuated at about 10^{-3} Torr. One pellet was annealed at 250 °C for 8 h, and the other annealed at 400 °C for 4 h, followed by air cooling. The pellet annealed at 250 °C was used to investigate the origin of the low intensity exothermic peak seen on the DSC thermogram at about 198 °C, without promoting the crystallization of amorphous phase. The other pellet, with the amorphous phase crystallized, was used to study the influence of the interfacial/amorphous component on the optical and photoacoustic properties.

Fig. 4 shows the XRD pattern for the pellet annealed at 250 °C. Besides the $FeSb_2$ and elemental Sb phases, new low intensity peaks located at about $2\theta = 35.2°$, 56.5° and 62.1° were observed and indexed to Fe_3O_4 (ICSD code 20596). Thus, the exothermic peak at about 198 °C seen on the DSC thermogram was attributed to the nucleation of Fe_3O_4. The XRD pattern was also refined, and the best fit was reached for the lattice parameters $a = 5.7547$ Å, $b = 6.4606$ Å, $c = 3.1723$ Å for $FeSb_2$; $a = 4.2554$ Å and $c = 11.1550$ Å for Sb; and $a = b = c = 8.35$ Å (8.4 Å) for Fe_3O_4. The value between parentheses is that provided by the ICSD code. The simulated patterns and residual intensity are also shown in Fig. 4, where an excellent agreement between simulated and experimental patterns can be seen. From the refinement, volume fractions of 67%, 23%, and 10% were obtained for $FeSb_2$, elemental Sb and Fe_3O_4, respectively. Annealing at 250 °C was not enough to crystallize the amorphous phase. Thus, is assumed that this annealed sample contains a volume fraction of 37% of the amorphous phase, as estimated previously. Maybe a partial crystallization occurred due to the long annealing time. Taking into account the volume fraction of the amorphous phase, volume fractions of 42.21%, 14.49% and 6.30% were obtained for $FeSb_2$, elemental Sb and Fe_3O_4, respectively. From the refinement, the β and 2θ values of the most intense peaks of $FeSb_2$, elemental Sb and Fe_3O_4 were used

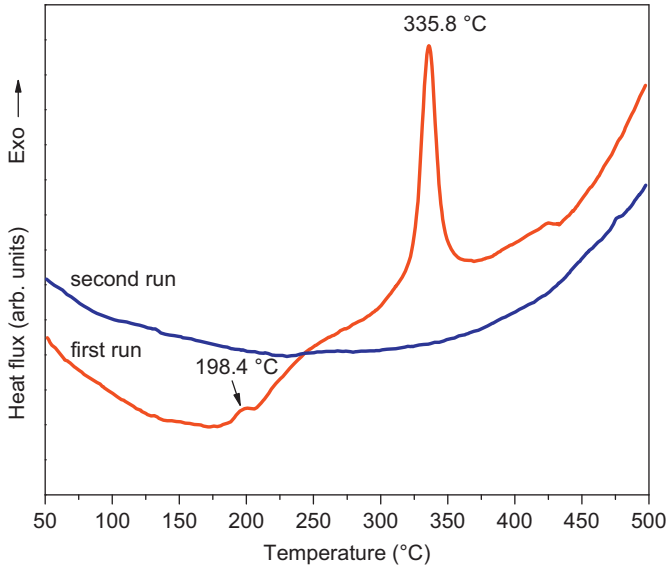

Fig. 2. DSC thermograms of a nanostructured powder milled for 32 h.

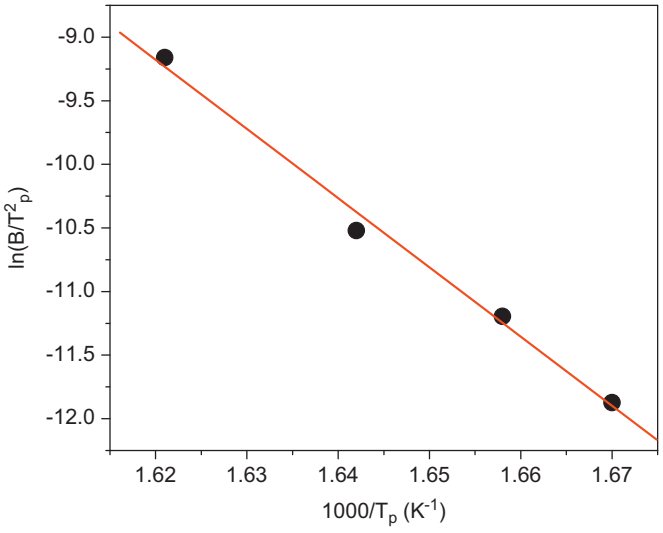

Fig. 3. Kissinger plot of $\ln(B/T^2)$ versus $1/T$ using the temperatures peaks mentioned in the text.

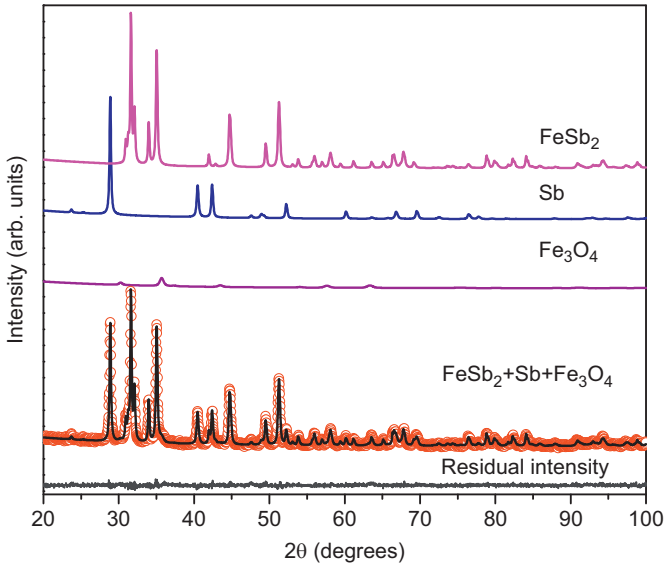

Fig. 4. Experimental (open circles) and simulated (solid lines) experimental XRD patterns of a nanostructured powder annealed at 250 °C.

in Eq. (1), and average crystallite size values of $D \approx 460$ Å, 312 Å and 152 Å, respectively, were obtained. For $FeSb_2$, the peaks mentioned previously were considered, while for Sb the peaks located at about 28.87°, 40.44° and 42.36° were considered and for Fe_3O_4, the peak located at about 35.71° was considered. The average crystallite size for $FeSb_2$ increased, while the volume fraction decreased significantly. An explanation for this apparent contradiction is the following: a sealed silica tube containing the sample was placed inside the oven and the temperature was gradually increased to 250 °C. This gradual increase in temperature promoted growth of crystallites up to a maximum value, before starting their decomposition. This maximum value was reached at a temperature smaller than 250 °C.

The annealing of an as-milled sample at 400 °C promoted crystallization of amorphous phase. Fig. 5 shows the XRD pattern for a pellet annealed at 400 °C (open circles). Only the same phases observed for the pellet annealed at 250 °C were seen. However, the intensities of diffraction peaks corresponding to the $FeSb_2$ phase decreased, while those corresponding to the elemental Sb phase increase significantly. The XRD pattern was refined and the best fit was reached for the lattice parameters $a=5.8716$ Å, $b=6.5934$ Å, $c=3.2424$ Å for $FeSb_2$; $a=4.3482$ Å and $c=11.3908$ Å for elemental Sb; and $a=b=c=8.4804$ Å for Fe_3O_4. The simulated patterns and residual intensity are also shown in Fig. 5, where an excellent agreement between simulated and experimental patterns can be seen. From the refinement, volume fractions of 30%, 44% and 26% for $FeSb_2$, elemental Sb and Fe_3O_4 were obtained, respectively. The β and 2θ values of most intense peaks for $FeSb_2$, elemental Sb and Fe_3O_4 were used in Eq. (1) and average crystallite size values of $D \approx 435$ Å, 650 Å and 390 Å, respectively, were obtained. The same peaks mentioned above were considered. These results corroborated the decomposition of $FeSb_2$ with increasing annealing temperature.

In order to further study the decrease of $FeSb_2$ with increasing annealing temperature, the XRD patterns of as-milled and annealed samples were converted to electron units using the procedure described in Refs. [34,35]. For converting each XRD pattern, a weighted theoretical mean square scattering factor $<f^2>_{aver}$ was calculated by considering the volume fractions of phases obtained from the refinement. Fig. 6 shows the XRD patterns converted to electron units. From this figure one can see that the volume fraction of $FeSb_2$ decreases with increasing annealing temperature, while those of elemental Sb and Fe_3O_4 increase. For $FeSb_2$, between $2\theta=30°$ and 33°, the integrated intensity values were 3901, 3394 and 2053 electron units for samples as-milled, annealed at 250 °C and annealed at 400 °C, respectively. The difference between the integrated intensities for samples as-milled and annealed at 400 °C is 1848 electron units, corresponding to a reduction of 47.4%. This value is similar to that calculated considering the volume fractions (48.8%).

Based on these results, the increase in the volume fraction of elemental Sb and the nucleation of Fe_3O_4 can be explained by following argument: annealing at 250 °C promotes the diffusion of Fe and Sb atoms located at the interfacial component as well as of those originated from the decomposition of $FeSb_2$. Thus, Sb atoms are incorporated into unreacted Sb crystallites, promoting their growth. On the other hand, the formation of Fe_3O_4 may be due to the fact that a small amount of oxygen remained inside the silica tubes after being evacuated and sealed. The enthalpy of formation of Fe_3O_4 is -1161.957 kJ mol^{-1} [40], which is very favorable to nucleation.

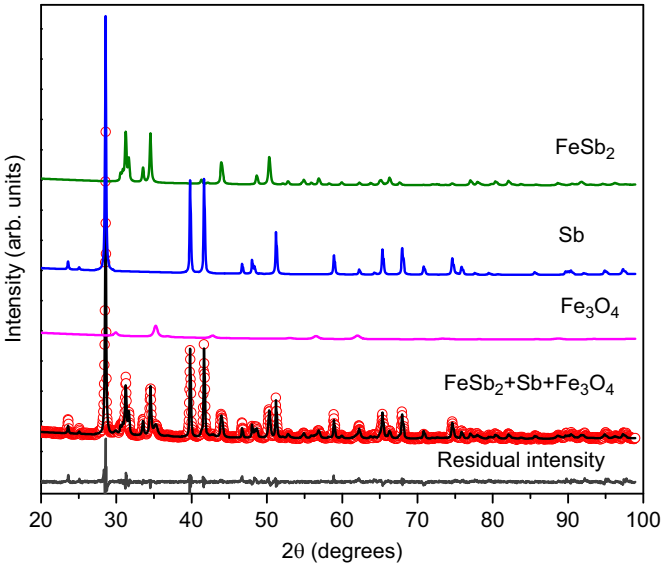

Fig. 5. Experimental (open circles) and simulated (solid lines) XRD patterns of a nanostructured powder annealed at 400 °C.

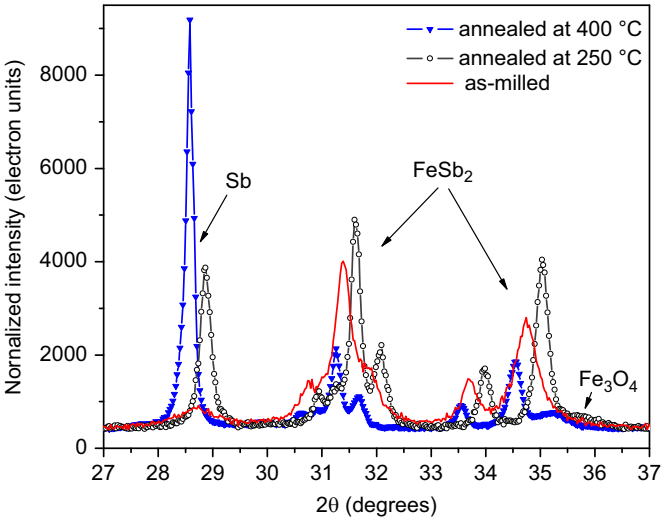

Fig. 6. XRD patterns of as-milled and annealed powders converted to electron units.

3.2. Determination of the band gap energy for as-milled and annealed $FeSb_2$

Fig. 7 shows the transmittance (Tr) spectra as a function of the light photon energy for samples as-milled and annealed at 400 °C. One can see that the spectrum of as-milled $FeSb_2$ shows a very large optical absorption edge due to the nanometric crystallite size, strains and a substantial interfacial/amorphous component. On the other hand, the spectrum for annealed $FeSb_2$ shows a narrow optical absorption edge due to grain growth and structural relaxation during the annealing process, but before decomposition. According to the literature, $FeSb_2$ has a direct optical band gap ($n=2$) at $E_g = 130$ meV and two indirect band gaps ($n=1/2$) at 6 and 31 meV [14], while for elemental Sb and Fe_3O_4 the optical band gap energies at 110 meV [41] and 140 meV [42], respectively.

The optical band gap energy can be obtained by a McClean analysis of the absorption edge through the equation [43]

$$\varepsilon\, h\upsilon = (h\upsilon - E_g + E_p)^{1/n} \tag{4}$$

where ε is the absorption coefficient, E_g is the optical band gap energy, E_p is the phonon energy for indirect transitions, h is the Planck constant and υ is the frequency of the incident beam. The analysis consists of fitting the absorption edge to Eq. (4) and determining experimental values for E_g, E_p and n. A value of $n=2$ implies a direct allowed transition; $n=2/3$ implies a direct forbidden transition; $n=1/2$ implies an indirect allowed transition; $n=1/3$ implies an indirect forbidden transition.

For transmittance measurements, as-milled and annealed powders were dispersed into a KBr powder support and the mixtures were pressed in the form of a pellet. In this case, the thickness l_s and the absorption coefficient ε of the samples are no longer known and Eq. (4) must be modified. Using the relationships $\varepsilon = A/l_s$, where A is the absorbance, and $A = \log_{10}(100/\%Tr)$ and replacing them in Eq. (4) gives

$$h\upsilon \log_{10}\frac{100}{\%Tr} = l_s(h\upsilon - E_g + E_p)^{1/n}, \tag{5}$$

where the thickness of the sample l_s is a parameter to be included in the fitting procedure.

Fig. 8 shows the fits to Eq. (5) of transmittance data for samples as-milled and annealed at 400 °C for direct allowed transition only. For the as-milled and annealed samples the direct band gap energies are $E_g = 125 \pm 0.24$ meV and 122 ± 0.24 meV, respectively. Due to broadening of the transmittance spectrum of both samples, the determination of the indirect band gap energies is very inaccurate. The direct band gap energy for the annealed sample is slightly smaller than that for the as-milled sample, since the average crystallite size is larger.

3.3. Raman measurements for as-milled and annealed $FeSb_2$ powders

Fig. 9 shows the RS spectra for samples as-milled and annealed at 400 °C. Both spectra show only a broad band between 140 and 200 cm^{-1}, which is sharper and stronger in the annealed sample. Raman peaks are broadened by defects (glide planes), amorphization, and intrinsic broadening when anharmonic processes are involved [44]. Due to the severe mechanical deformations imposed by mechanical collisions with the steel balls during MA, all the characteristics mentioned above are found in nanostructured materials. The line narrowing and the increase in band intensity are attributed to the annealing process, since it promotes crystallite growth of the $FeSb_2$ phase.

Under ambient conditions, Sb crystallizes in the D^5_{3d} symmetry (S.G. $R\bar{3}m$) and has two Raman active modes: A_{1g} at 150 cm^{-1} and two-fold degenerated E_g at 115 cm^{-1} [45]. Fe_3O_4 crystallizes in the O^7_h symmetry (S.G. $Fd\bar{3}m$) and its Raman active modes are T^1_{2g} at 192 cm^{-1}, E_g at 308.5 cm^{-1}, T^2_{2g} at 541.2 cm^{-1} and A_{1g} at 672.3 cm^{-1} [46]. In Fig. 9, the low intensity peak located at about 121 cm^{-1} (full square) is attributed to the E_g modes of Sb, while the A_{1g} mode is located within the intense broad band. The identification of the Raman active modes of Fe_3O_4 is very hard. The low intensity broad band at about 270 cm^{-1} (asterisk) was not identified. According to the RRUFF Database (code ID-R070383) [45], $FeSbO_4$ (tripuhyite) shows a Raman active mode at about 280 cm^{-1}. However, this phase was not found in the XRD patterns of samples annealed at 250 °C and 400 °C.

The normal modes of orthorhombic $FeSb_2$ at the Γ point of the Brillouin zone are classified according to the irreducible representations of this point group [47].

$$\Gamma = 2A_g + 2B_{1g} + B_{2g} + B_{3g} + B_{1u} + 3B_{2u} + 3B_{3u} \tag{6}$$

where g and u denote Raman active and infrared modes, respectively.

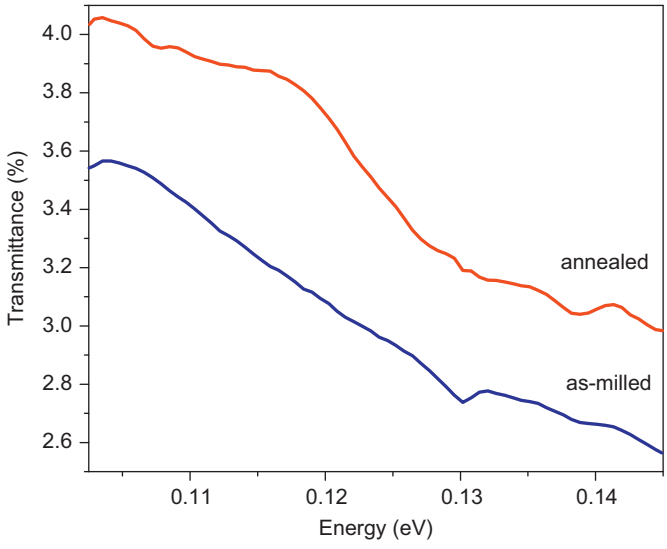

Fig. 7. Optical transmittance spectra versus energy of as-milled and annealed powders.

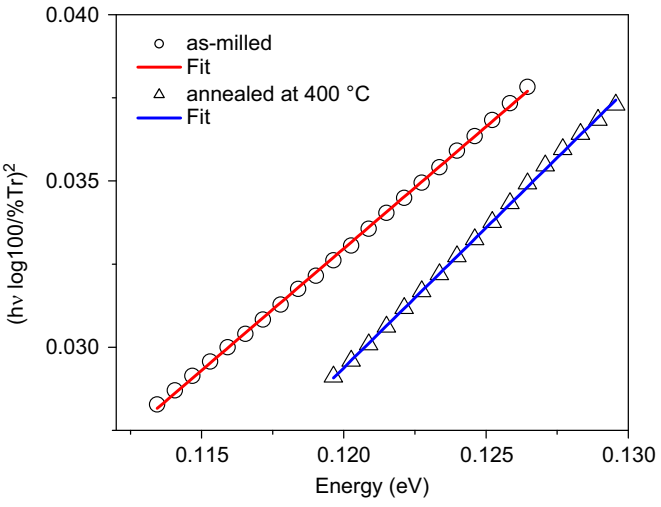

Fig. 8. Determination of direct optical band gap energies for samples as-milled and annealed at 400 °C. The solid lines correspond to the best fits of Eq. (5) to the experimental data.

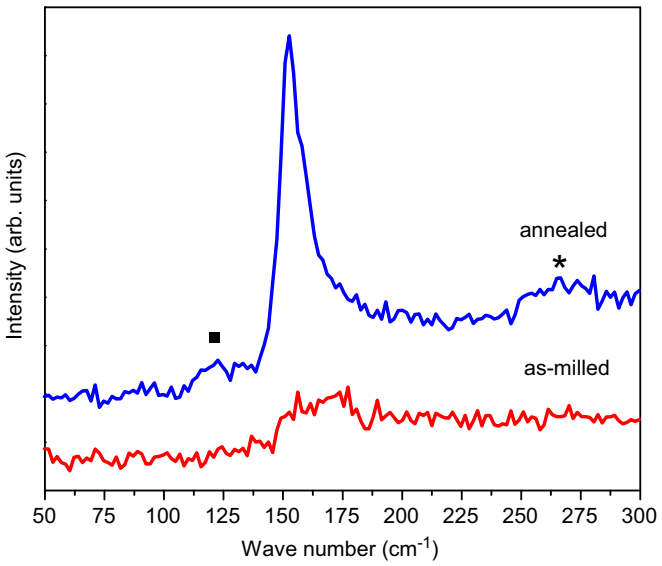

Fig. 9. Raman spectra of as-milled and annealed powders. The excitation wavelength was $\lambda = 514.5$ nm. Raman active modes of Sb (full square) and unidentified (asterisk) are also shown.

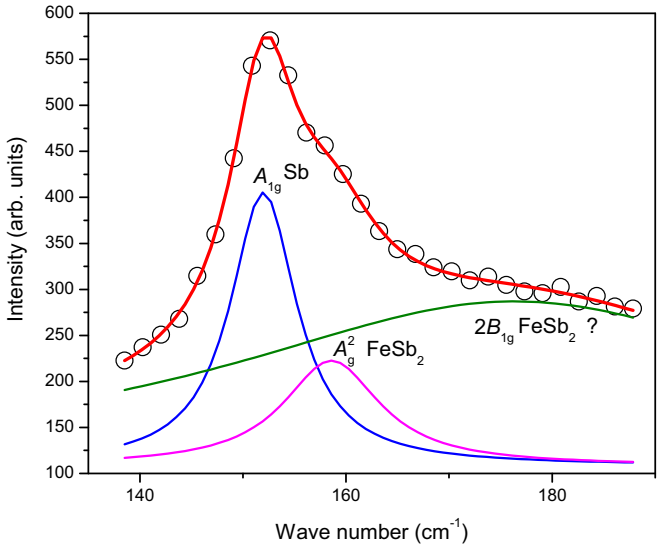

Fig. 10. Deconvolution of Raman spectrum for samples annealed at 400 °C.

Lazarevic et al. [47] reported the RS spectrum for orthorhombic $FeSb_2$ at room temperature, and the wave numbers are: A_g^1 at 146.8 cm^{-1}, A_g^2 at 161.2 cm^{-1}, B_{1g}^1 at 173.3 cm^{-1}, B_{1g}^2 at 184.3 cm^{-1}, B_{2g} at 89.4 cm^{-1} and B_{3g} at 95.6 cm^{-1}. The wave number values for the IR modes are also given in Ref. [47].

The intense broad band seen on the RS spectrum for the annealed samples was deconvoluted using Lorentzian functions, and the results are shown in Fig. 10. From the deconvolution, the peak at about 151 cm^{-1} was attributed to A_{1g}mode of elemental Sb, while that at 159 cm^{-1} was attributed to A_g^2 mode of $FeSb_2$. The broad peak was attributed to fluorescence, and maybe the two-fold degenerated $2B_{1g}$ are overlapped. The A_{1g}, A_g^2 and B_{1g}^2 modes were observed in Ref. [30].

3.4. Photoacoustic measurements for as-milled and annealed $FeSb_2$ powders

The photoacoustic absorption spectroscopy theory and its application to determine the thermal diffusivity parameter and/or transport properties of semiconductor materials are widely documented in literature [48–50]. A review can be found in some papers [35,51] as well as in references therein and it will not be repeated here.

The thermal diffusivity for orthorhombic $FeSb_2$ can be calculated using the expression for the thermal conductivity $k = \rho\, C_p\, \alpha_s$, where ρ is the density, C_p is the specific heat, and α_s is the thermal diffusivity. The TAPP software (version 2.2) [40] gives values of $\rho = 8151\ kg\ m^{-3}$ and $C_p = 228\ J\ kg^{-1}\ K^{-1}$ for $FeSb_2$. Sun et al. [52] reported a value of $k = 8\ W\ m^{-1}\ K^{-1}$ for $FeSb_2$ at ambient conditions. Using these values in the expression above, a value of $\alpha_s = 0.043\ cm^2\ s^{-1}$ is obtained. The characteristic frequency $f_c = \alpha_s/\pi\, l_s^2$, where l_s is the sample thickness, is the modulation frequency corresponding to the transition from the thermally thin regime ($f < f_c$) to the thermally thick regime ($f > f_c$). The thicknesses of as-milled and annealed samples were 425 and 500 μm, giving characteristic frequencies of 7.6 Hz and 5.5 Hz, respectively. In order to perform PAS measurements in the thermally thick regime, the data were acquired between 10 and 270 Hz.

Fig. 11 shows the $\log S$ versus $\log f$ plot of PAS signal amplitudes for samples as-milled and annealed at 400 °C, while the phases are displayed in Fig. 12. One can see that the effect of annealing was to promote a reduction in the signal amplitude up to 35 Hz. On the other hand, annealing promoted a reduction in phase for the modulation frequency range used, as shown in Fig. 12.

The $\log S$ versus $\log f$ plot of signal amplitude for as-milled samples shows modulation frequency dependence $\approx f^{-1.00}$ between 45 and 140 Hz, while the dependence for annealed samples is $\approx f^{-0.95}$ between 29 and 95 Hz. A dependence of the type $\approx f^{-1.00}$ is characteristic of nonradiative surface recombination, thermoelastic bending or thermal dilation [53]. Thermal dilation produces a signal whose phase is independent of the modulation frequency and equal to $-90°$. As shown in the Fig. 11, this behavior is not observed, allowing us to disregard this heat transfer mechanism. The absence of thermoelastic bending was verified by it not being possible to fit the phase data to the phase Eq. (4) given in Ref. [35], using $\alpha = 0.043\ cm^2\ s^{-1}$ as the initial value for the thermal diffusivity.

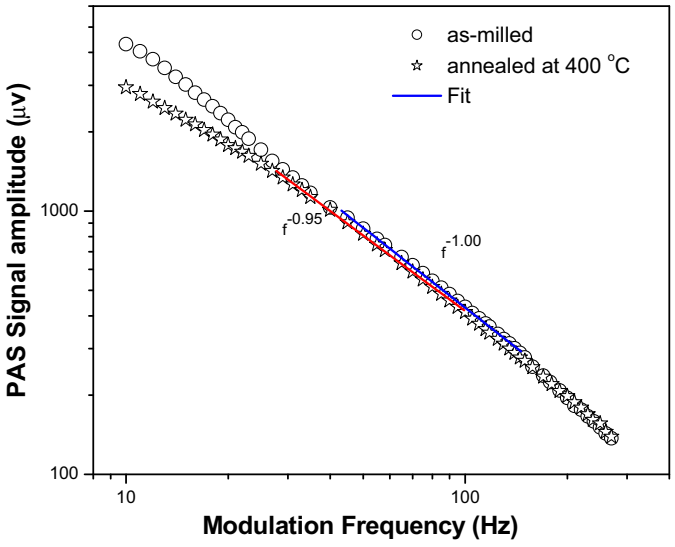

Fig. 11. PAS signal amplitude versus modulation frequency of as-milled and annealed powders. The solid lines are linear fits.

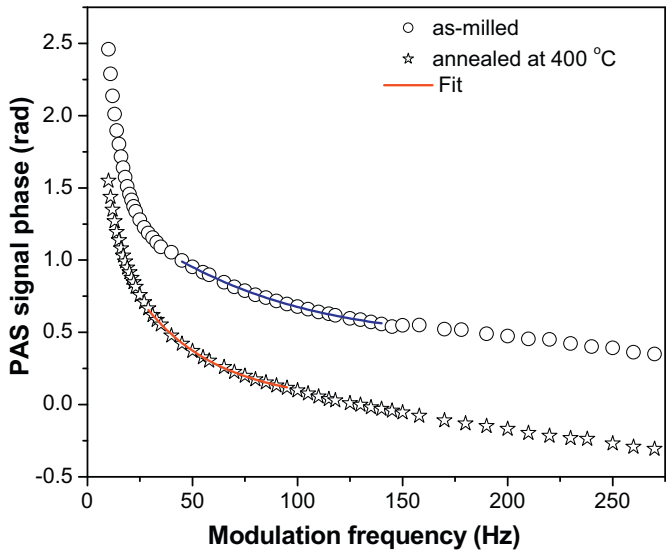

Fig. 12. PAS signal phase versus modulation frequency of as-milled and annealed powders. The solid lines correspond to the best fits of Eq. (7) to the experimental data.

The expression for the phase corresponding to the nonradiative surface recombination is given by Pinto-Neto et al. [50],

$$\Phi_{ph} = \frac{\pi}{2} + \tan^{-1}\left[\frac{(bD/v)(\omega\tau_{eff}+1)}{(bD/v)(1-\omega\tau_{eff})-1-(\omega\tau_{eff})^2}\right] \quad (7)$$

where $\tau_{eff}=\tau(D/\alpha_s-1)$, $b=(\pi f/\alpha_s)^{1/2}$, $\omega=2\pi f$, α_s is the thermal diffusivity, D is the carrier diffusion coefficient, v is the surface recombination velocity, and τ is the recombination time. The expression (7) was successfully fitted to the plot Φ_{ph} (radians) versus f in the modulation frequency range 45–140 Hz for as-milled samples for the values $\alpha_s=0.0786\pm0.0001$ cm^2 s^{-1}, $D=33.788\pm0.027$ cm^2 s^{-1}, $v=155.445\pm0.124$ cm s^{-1} and $\tau=652\pm9$ ns and for annealed sample in the frequency range 29–95 Hz for the values $\alpha_s=0.0847\pm0.0002$ cm^2 s^{-1}, $D=82.806\pm0.093$ cm^2 s^{-1}, $v=238.211\pm0.268$ cm s^{-1} and $\tau=256\pm7$ ns. The thermal diffusivity of both as-milled and annealed samples is almost twice the value previously calculated for $FeSb_2$. In another study, we reported the results obtained for a nominal $CoSb_3$ mixture submitted to the MA process [54]. After 30 h of milling, the Rietveld analysis of the XRD pattern for as-milled powder showed a microstructure formed by the skutterudite $CoSb_3$ and monoclinic $CoSb_2$ nanostructured phases and an interfacial component. The photoacoustic properties of the as-milled and annealed powders were investigated. From the PAS data for the as-milled powder, the intraband nonradiative thermalization (thermal diffusion) and thermoelastic bending mechanisms were observed. From the PAS data for the annealed powder, besides the heat transfer mechanisms mentioned early, the nonradiative surface recombination mechanism was observed. The latter permitted the determination of the transport properties. Due to the similarity between the Fe–Sb and Co–Sb systems, in order to fit the theoretical results to the experimental curve, we fixed the $\alpha=0.043$ cm^2 s^{-1} value calculated previously for $FeSb_2$ and the D, v, and τ values given in Ref. [54] were taken as initial data. After an initial convergence, all the parameters were kept as free parameters.

The microstructure of samples annealed at 400 °C is composed by 30%, 44% and 26% of $FeSb_2$, elemental Sb and Fe_3O_4, respectively. The thermal diffusivity values of elemental Sb and Fe_3O_4 can be calculated using data given in the softwares PTOE [55] and TAPP [40]. The software PTOE gives the values $k=24.3$ W m^{-1} K^{-1}, $\rho=6684$ kg m^{-3} and $C_p=210$ J kg^{-1} K^{-1} for elemental Sb. Using these values in the expression for the thermal conductivity, a value of $\alpha_{Sb}=0.173$ cm^2 s^{-1} was obtained. The software TAPP [40] gives the values $\rho=1305$ kg m^{-3} and $C_p=636$ J kg^{-1} K^{-1} for Fe_3O_4, while Ref. [56] reports a value of $k=5$ W m^{-1} K^{-1}. Using these values in the expression for the thermal conductivity, a value of $\alpha_{Fe_3O_4}=0.0602$ cm^2 s^{-1} was obtained.

It will be assumed that the measured thermal diffusivity α_s for samples annealed at 400 °C is described by the Lichtenecker's logarithmic mixture law [57,58],

$$\alpha_{eff} = \prod_{n=1}^{3} \alpha_n^{x_n} \quad (8)$$

where n is the number of phases; x and α are the volume fraction and thermal diffusivity of each phase, respectively. Using the volume fractions and thermal diffusivity values calculated previously for $FeSb_2$, elemental Sb and Fe_3O_4 in Eq. (8), a value of $\alpha_{eff}=0.0866$ cm^2 s^{-1} was obtained. This value is very close to the measured value ($\alpha_s=0.0847$ cm^2 s^{-1}).

The Lichtenecker's logarithmic mixture law was used to investigate the contribution of interfacial/amorphous component for the thermal diffusivity of the as-milled samples. From refinement of the XRD pattern of as-milled samples, volume fractions of $x_n=58.6\%$, 4.4% and 37% were estimated for the $FeSb_2$, Sb and interfacial/amorphous components, respectively. Considering the thermal diffusivity values calculated for $FeSb_2$ and elemental Sb and their volume fractions in Eq. (8), a value of $\alpha_{int+am}=0.186$ cm^2 s^{-1} for the interfacial/amorphous component is obtained. If it is assumed that the measured thermal diffusivity is a weighted sum of the thermal diffusivities of $FeSb_2$ and elemental Sb, a value of $\alpha_{int+am}=0.124$ cm^2 s^{-1} for the interfacial/amorphous component is obtained. Both calculated values for interfacial/amorphous component are at least three times the value of thermal diffusivity for bulk $FeSb_2$.

Thermal transport in nanostructured materials has been extensively studied both theoretically and experimentally. Eastman et al. [59,60] investigated the effects of energy carrier (phonon) scattering on thermal transport within nanograins and on thermal transport across the nanograin interface. They studied the variation of the effective thermal conductivity of nanocrystalline zirconia with the size of nanograins and temperature, and reported a reduced thermal conductivity of the nanograin itself due to phonon scattering at the grain interface. Philip et al. [61] reported results for nanocrystalline diamond films grown by chemical vapor deposition (CVD). They reported that the thermal diffusivity for $\approx$ 3.5-μm-thick nanocrystalline diamond films with nucleation densities $\geq 10^{12}$ cm^{-2} (smaller interfacial component) was ≈ 7.2 cm^2 s^{-1}, whereas those with lower nucleation densities (larger interfacial component) showed a value of ≈ 5.5 cm^2 s^{-1}. These results show that the nanometric dimensions of crystallites (crystalline component) and the defect concentration (interfacial component) decrease the thermal conductivity and thermal diffusivity of nanostructured materials.

In this study, the interfacial/amorphous component seems to be responsible for the fact that the thermal diffusivity of as-milled samples is larger than that calculated for bulk $FeSb_2$. For both as-milled and annealed samples, the heat transfer mechanism found was the nonradiative surface recombination, i.e., after diffusion, the recombination of excess electron–hole pairs occurs at the surface. Physically, the arguments to explain the large thermal diffusivity of as-milled samples are the following: (1) the generated excess electron–hole pairs may diffuse several hundreds of nanometers before recombining; and/or (2) the density of phonons confined in the interfacial component is very high, allowing a strong phonon-phonon interaction promoting the heat transport.

4. Conclusions

A stoichiometric $FeSb_2$ mixture was submitted to mechanical milling, and after 32 h of milling the XRD pattern was indexed to orthorhombic $FeSb_2$ and elemental Sb. In addition, an amorphous phase was observed. From refinement of the XRD patterns for as-milled and annealed samples, a decrease in volume fraction for $FeSb_2$ with increasing annealing temperature was observed, the volume fractions of elemental Sb and Fe_3O_4 increased.

From transmittance VIS–IR measurements, the direct optical band gap energies of samples as-milled and annealed at 400 °C were determined, and a value slightly smaller was observed for annealed samples due to a larger average crystallite size.

From the PAS measurements, the thermal diffusivities and other transport properties of samples as-milled and annealed at 400 °C were determined. The thermal diffusivity of the annealed samples is well described by the Lichtenecker's logarithmic mixture law. The large thermal diffusivity value for the as-milled sample is attributed to the contribution of the thermal diffusivity of the interfacial/amorphous component.

Acknowledgments

The authors thank the Brazilian agencies CNPq, CAPES and FAPESC for financial support. They are also indebted to the UFSC Bio-inorganic, Crystallography and Raman Spectroscopy laboratories.

References

[1] S. Paschen, in Thermoelectric Handbook, in: D.M. Rowe (Ed.), CRC Press, Taylor & Francis, Boca Raton, 2006, Chap. 15.
[2] G.D. Mahan, B. Sales, J. Sharp, Phys. Today 50 (1997) 42.
[3] Y. Sun, S. Canulescu, P. Sun, F. Steglich, N. Pryds, J. Schou, B.B. Iversen, Appl. Phys. A 104 (2011) 883.
[4] Y. Hadano, S. Narazu, M.A. Avila, T. Onimaru, T. Takabatake, J. Phys. Soc. Jpn. 78 (2008) 013702.
[5] B.C. Sales, E.C. Jones, B.C. Chakoumakos, J.A. Fernandez-Baca, H.E. Harmon, J.W. Sharp, E.H. Volckmann, Phys. Rev. B 50 (1994) 8207.
[6] A. Bentien, S. Johnsen, G.K.H. Madsen, B.B. Iversen, F. Steglich, Europhys. Lett. 80 (2007) 17008.
[7] G. Wertheim, V. Jaccarino, J. Wernick, J. Seitchik, H. Williams, R. Sherwood, Phys. Lett. 18 (1965) 89.
[8] V. Jaccarino, G.K. Wertheim, J.H. Wernick, L.R. Walker, S. Arajs, Phys. Rev. 160 (1967) 476.
[9] D. Mandrus, J.L. Sarrao, A. Migliori, J.D. Thompson, Z. Fisk, Phys. Rev. B 51 (1995) 4763.
[10] Y. Takahashi, T. Moriya, J. Phys. Soc. Jpn. 46 (1979) 1451.
[11] R. Hu, V.F. Mitrovic, C. Petrovic, Phys. Rev. B 74 (2006) 195130.
[12] V.I. Anisimov, S.Y. Ezhov, I.S. Elfimov, I.V. Solovyev, T.M. Rice, Phys. Rev. Lett. 76 (1996) 1735.
[13] S. Paschen, E. Felder, M.A. Chernikov, L. Degiorgi, H. Schwer, H.R. Ott, D.P. Young, J.L. Sarrao, Z. Fisk, Phys. Rev. B 56 (1997) 12916.
[14] A. Herzog, M. Marutzky, J. Sichelschmidt, F. Steglich, Phys. Rev. B 82 (2010) 245205.
[15] M.S. Diakhate, R.P. Hermann, A. Mochel, I. Sergueev, M. Sondergaard, M. Christensen, M.J. Verstraete, Phys. Rev. B 84 (2011) 125210.
[16] R. Hu, V. Mitrovic, C. Petrovic, Appl. Phys. Lett. 92 (2008) 182108.
[17] R. Hu, V.F. Mitrovic, C. Petrovic, Phys. Rev. B 76 (2007) 115105.
[18] C. Petrovic, Y. Lee, T. Vogt, N.D. Lazarov, S.L. Bud'ko, P.C. Canfield, Phys. Rev. B 72 (2005) 045103.
[19] A. Bentien, G.K.H. Madsen, S. Johnsen, B.B. Iversen, Phys. Rev. B 74 (2006) 205105.
[20] Inorganic Crystal Structure Database (Gmelin-Institut fur Anorganische Chemie and Fachinformationszentrum FIZ, Karlsruhe, 1995); Joint Committee on Powder Diffraction Standards (Philadelphia, 2000).
[21] P.C. Canfield, Z. Fisk, Philos. Mag. B 65 (1992) 1117.
[22] P. Amornpitoksuk, S. Suwanboon, T. Ratana, T. Ratana, J. Alloys Compd. 501 (2010) 100.
[23] S. Ur, P. Nash, I. Kim, J. Mater. Sci. 38 (2003) 3553.
[24] C. Suryanarayana, Prog. Mater. Sci. 46 (2001) 1.
[25] J.C. de Lima, D.M. Trichês, V.H.F. dos Santos, T.A. Grandi, J. Alloys Compd. 282 (1999) 258.
[26] R.B. Schwarz, R.R. Petrich, C.K. Saw, J. Non-Cryst. Solids 76 (1985) 281.
[27] H.J. Fecht, Acta Metall. Mater 38 (1990) 1927.
[28] J.C. de Lima, V.H.F. dos Santos, T.A. Grandi, P.C.T. D'Ajello, A. Dmitriev, Phys. Rev. B 62 (2000) 8871.
[29] H. Gleiter, Nanostruct. Mater. 1 (1992) 1.
[30] C.M. Poffo, S.M. Souza, D.M. Trichês, J.C. de Lima, T.A. Grandi, A. Polian, M. Gauthier, Physica B 407 (2012) 4686.
[31] J.C. de Lima, N. cella, L.C.M. Miranda, C. Chying An, A.H. Franzan, N.F. Leite, Phys. Rev. B 46 (1992) 14186.
[32] H.M. Rietveld, J. Appl. Cryst. 2 (1969) 65.
[33] A.C. Larson, R.B. Von Dreele, Los Alamos National Laboratory Report LAUR 86, 2004.
[34] C.M. Poffo, J.C. de Lima, S.M. Souza, D.M. Trichês, T.A. Grandi, R.S. de Biasi, J. Raman Spectrosc. 41 (2010) 1316.
[35] S.M. Souza, D.M. Trichês, J.C. de Lima, T.A. Grandi, R.S. de Biasi, Physica B 405 (2010) 2807.
[36] H.P. Klug, L.E. Alexander, X-ray Diffraction Procedures, 2nd edition, John Wiley & Sons, Inc., New York, USA, 1974.
[37] H.E. Kissinger, Annal. Chem. 29 (1957) 1702.
[38] J.A. Augis, J.E. Bennett, J. Therm. Anal. 13 (1978) 283.
[39] Microcal Origin version 6, Microcal Software, Inc., Northampton, MA.
[40] TAPP Software, Version 2.2, Wade Court, Hamilton, OH, E. S. Microwave, Inc.
[41] T.J. Fox, R.P. Howson, D.C. Emmony, J. Phys. D: Appl. Phys. 7 (1974) 1864.
[42] S.K. Park, T. Ishikawa, Y. Tokura, Phys. Rev. B 58 (1998) 3717.
[43] T.P. McLean, Prog. Semicond. 5 (1960) 55.
[44] G. Lucazeau, J. Raman Spectrosc. 34 (2003) 478.
[45] RRUFF Database, available from 〈http://rruff.info/〉.
[46] J. Zhang, P.H. Tan, W. Zhao, J. Lu, J.H. Zhao, J. Raman Spectrosc. 42 (2011) 1388.
[47] N. Lazarevic, M.M. Radonjic, D. Tanaskovic, R. Hu, C. Petrovic, Z.V. Popovic, J. Phys.: Condens. Matter. 24 (2012) 255402.
[48] A. Rosencwaig, A. Gersho, J. Appl. Phys. 47 (1976) 64.
[49] H. Vargas, L.C.M. Miranda, PHYSICS REPORTS (Review Section of Physics Letters), 161, North-Holland, Amsterdam, 1988, p. 43–101.
[50] A. Pinto-Neto, H. Vargas, N.F. Leite, L.C.M. Miranda, Phys. Rev. B 41 (1990) 9971.
[51] C.M. Poffo, J.C. de Lima, S.M. Souza, D.M. Trichês, T.A. Grandi, R.S. de Biasi, Physica B 406 (2011) 1627.
[52] P. Sun, N. Oeschler, S. Johnsen, B.B. Iversen, F. Steglich, 25th International Conference on Low Temperature Physics (LT25) Journal of Physics: Conference Series 150, (2009) p. 012049.
[53] G. Rousset, F. Lepoutre, L. Bertrand, J. Appl. Phys. 54 (1983) 2383.
[54] D.M. Trichês, J.C. de Lima, S.M. Souza, C.M. Poffo, T.A. Grandi, R.S. de Biasi, J. Appl. Phys. 110 (2011) 083528.
[55] PTOE Software, available at 〈www.chemglobe.org/ptoe〉.
[56] G.A. Slack, Phys. Rev. B 126 (1962) 427.
[57] K. Lichtenecker, Phys. Zeitschr (115) , Vol. XXVII.
[58] R. Simpkin, IEEE Transactions on Microwave Theory and Techniques 58 (No. 3) (2010), March.
[59] G. Soyez, J.A. Eastman, L.J. Thompson, G.-R. Bai, P.M. Baldo, A.W. McCormick, R.J. DiMelfi, A.A. Elmustafa, M.F. Tambwe, D.S. Stone, Appl. Phys. Lett. 77 (2000) 1155.
[60] H. Yang, G.R. Bai, L.J. Thompson, J.A. Eastman, Acta Mater. 50 (2002) 2309.
[61] J. Philip, P. Hess, J.E. Bulter, S. Chattopadhyay, K.H. Chen, L.C. Chen, J. Appl. Phys. 93 (2003) 2164.